Physica Status Solidi A: Applications and Materials Science
Efficiency improvements in solution-based CuInS2 solar cells incorporating a Cl-doped ZnO nanopillars array
--Manuscript Draft--

Manuscript Number:	pssa.201700191R3
Full Title:	Efficiency improvements in solution-based CuInS2 solar cells incorporating a Cl-doped ZnO nanopillars array
Article Type:	Original Paper
Section/Category:	
Keywords:	inorganic solar cell; solution-based techniques; nanopillars; Cl:ZnO; CuInS2
Corresponding Author:	Mariana Berruet, Ph.D Instituto de Investigaciones en Ciencia y Tecnologia de Materiales ARGENTINA
Corresponding Author Secondary Information:	
Corresponding Author's Institution:	Instituto de Investigaciones en Ciencia y Tecnologia de Materiales
Corresponding Author's Secondary Institution:	
First Author:	Yesica Di Iorio, Ph.D
First Author Secondary Information:	
Order of Authors:	Yesica Di Iorio, Ph.D
	Mariana Berruet, Ph.D
	Daniel Gau
	Enzo Spera
	Javier Pereyra
	Ricardo Marotti
	Marcela Vazquez
Order of Authors Secondary Information:	
Abstract:	Solar cells were prepared combining ZnO as n-type win-dow, In2S3 as buffer layer and CuInS2 as p-type absorbing layer. Superstrate configuration was chosen so that all the materials could be prepared using inexpensive and eco-friendly techniques based on solution processed deposition methods and non-toxic materials, avoiding vacuum, high temperature, Cd-containing layers and KCN purification stages. Also, no further sulfurization treatment is involved in the preparation. To improve the collection efficiency, cells were built using two different ZnO nanostructures (with and without Cl-doping), and compared to the re-sponse a cell prepared with just one dense ZnO layer. The photoresponse of the three different solar cells was ana-lysed by J-V curves under illumination and intensity-modulated photovoltage/photocurrent spectroscopy. A systematic characterization of the morphology and composition was carried out using X-ray diffraction, Raman confocal and electronic microscopy. The introduction of a nanostructured layer is not enough to produce a marked improvement in any of the electrical parameters. Instead, the presence of Cl-doped nanopillars is shown to increase the efficiency of the solar cells up to a maximum value of 2.8%. A better series resistance together with a higher value for the charge collection efficiency contributes to explain the corresponding improvement in cell efficiency.
Additional Information:	
Question	Response
Please submit a plain text version of your	Mar del Plata, September 4, 2017

cover letter here. Please note, if you are submitting a revision of your manuscript, there is an opportunity for you to provide your responses to the reviewers later; please do not add them to the cover letter.	Stefan Hildebrandt Editor-in-chief Physica Status Solidi (a) Please find enclosed the revised manuscript "Efficiency improvements in solution-based CuInS2 solar cells incorporating a Cl-doped ZnO nanopillars array" by Y. Di Iorio, M. Berruet, D. L. Gau, E.L. Spera, C. J. Pereyra, R.E. Marotti, M. Vázquez. I would greatly appreciate if you would consider it for publication in Physica Status Solidi (a). The article is original, unpublished and not being considered for publication elsewhere. In this manuscript, we describe the preparation of solar cells in superstrate configuration combining ZnO as n-type transparent window, In2S3 as buffer layer and CuInS2 (CIS) as p-type absorbing layer. These cells were prepared using eco-friendly processes and non-toxic materials, avoiding vacuum, high temperature heat treatments, Cd-containing layers and KCN purification stages. Three different ZnO layers were compared, including one dense and compact and two nanostructured layers, with and without Cl-doping. After a detailed characterization, we are able to demonstrate that the presence of Cl-doped nanopillars induces an increase the efficiency of the solar cells up to a maximum value of 2.8%. Reply to reviewer was added. I thank you in advance. Sincerely, Dr. Mariana Berruet
Do you or any of your co-authors have a conflict of interest to declare?	No. The authors declare no conflict of interest.

Efficiency improvements in solution-based CuInS$_2$ solar cells incorporating a Cl-doped ZnO nanopillars array

Y. Di Iorio[1], M. Berruet[*,1], D. L. Gau[2], E.L. Spera[2], C. J. Pereyra[2], R.E. Marotti[2], M. Vázquez[1]

[1] División Electroquímica Aplicada, INTEMA, Facultad de Ingeniería, CONICET-Universidad Nacional de Mar del Plata, J.B. Justo 4302, B7608FDQ Mar del Plata, Argentina

[2]Instituto de Física and CINQUIFIMA, Facultad de Ingeniería, Universidad de la República,Julio Herrera y Reissig565, C.C. 30, 11000 Montevideo, Uruguay

* Corresponding author: mberruet@fi.mdp.edu.ar, Phone: +54 223 481 6600, Fax: +54 223 481 0046

Solar cells were prepared combining ZnO as n-type window, In$_2$S$_3$ as buffer layer and CuInS$_2$ as p-type absorbing layer. Superstrate configuration was chosen so that all the materials could be prepared using inexpensive and eco-friendly techniques based on solution processed deposition methods and non-toxic materials, avoiding vacuum, high temperature, Cd-containing layers and KCN purification stages. Also, no further sulfurization treatment is involved in the preparation. To improve the collection efficiency, cells were built using two different ZnO nanostructures (with and without Cl-doping), and compared to the response a cell prepared with just one dense ZnO layer. The photoresponse of the three different solar cells was analysed by *J-V* curves under illumination and intensity-modulated photovoltage/photocurrent spectroscopy. A systematic characterization of the morphology and composition was carried out using X-ray diffraction, Raman confocal and electronic microscopy. The introduction of a nanostructured layer is not enough to produce a marked improvement in any of the electrical parameters. Instead, the presence of Cl-doped nanopillars is shown to increase the efficiency of the solar cells up to a maximum value of 2.8%. A better series resistance together with a higher value for the charge collection efficiency contributes to explain the corresponding improvement in cell efficiency.

1 Introduction Solar cells based on chalcopyrite materials, namely CuInS$_2$ (CIS), CuInSe$_2$ (CISe) and Cu(In,Ga)Se$_2$ (CIGS), draw permanent attention because their excellent optical properties turn them into well suited absorbers for solar cells [1, 2]. At the same time, ZnO has also been extensively employed as n-type semiconductor or window layer both in inorganic and hybrid solar cells [3, 4]. Although these materials are mainly prepared using high vacuum techniques, solar cells built with solution-based methods that combine chalcopyrites and ZnO are not uncommon, and their efficiency has been increasing steadily over the last years [5-16]. Various deposition methodologies have been used, such as electrodeposition [5, 11], spraying [12-14] and solution growth techniques [10]. However, many of these cells are prepared in substrate configuration and involve a layer of toxic CdS or a stage involving hazardous hidrazine or require a thermal treatment in highly toxic H$_2$S atmosphere. This is the case of the (so far) highest performance hydrazine-based solution processed device with certified power conversion efficiency (PCE) of 17.3%, based on a composition grading profile of CIGS absorber layer and a CdS buffer layer [15]. Superstrate cells usually show lower efficiencies but are still interesting concept proofs for applications such as tandem, flexible or bifacial cells. Dehghani, Cheshme Khavar and co-authors have recently reported various totally solution processed CuInS$_2$ solar cells in superstrate configuration [6-9]. These cells are composed of

FTO/TiO$_2$/In$_2$S$_3$/CIS/carbon, where all the layers are compact films (no nanostructured layer is included). Conversion efficiencies reach values close to 3% with CIS inks synthesized using a hot injection process [8], up to 5.2% for CIS inks deposited by spin coating [7, 9] and 2.67% when all the layers are deposited by spin coating of molecular precursor inks [6].

On the other hand, the incorporation of nanostructures can be used to partially compensate the typically low efficiencies of superstrate cells. The introduction of nanostructured layers has been analyzed before in an effort to minimize charge loss by increasing the interfacial area [17]. Moreover, it has been suggested that the requirements on the minority carrier diffusion length of the absorber material are reduced significantly in comparison to a planar geometry [18-20]. Kärber et al. [16] reported a nanostructured ZnO/In$_2$S$_3$/CuInS$_2$ superstrate solar cell with all the layers deposited by chemical spray pyrolysis, where the introduction of nano-columnar ZnO increased the conversion efficiency from 2 to 3%. In our recent paper, nanopillars of ZnO have been doped with chloride ions to increase the free electron density [21]. The present work focuses on the positive influence of this chloride-doped nanostructed ZnO layer on the efficiency of a photovoltaic solar cell.

Solar cells in superstrate configuration combining chloride-doped nanostructed ZnO as n-type transparent window, In$_2$S$_3$ as buffer layer and CIS as p-type absorbing layer were prepared and evaluated. The mere introduction of a nanostructured layer was not enough to produce a marked improvement in the relevant electrical parameters. The differences become significant only when nanostructed ZnO is doped with Cl. The porous nature of the ZnO nanopillars together with the lower resistance and higher electron densities provided by chloride doping, plus the cyclic character of the spin coating, contributed to form a pn junction which is distributed in space and increases the efficiency of the solar cell. It is also worth noting that there was no need to include further etching stages with toxic KCN solutions, which are frequently necessary to eliminate undesired secondary phases present in the CIS layer [22, 23]. Also, the buffer layer chosen was Cd-free and no further sulfurization treatment was applied.

2 Material and methods

2.1 Substrate The cells were prepared in superstrate configuration using FTO (fluorine doped tin oxide, supplied by Zhuhai Kaivo Electronic Components Co., Ltd.) as substrate. FTO sheets were cut into rectangular pieces of 1 × 3 cm^2 and cleaned in an ultrasonic bath with acetone and ethanol.

2.2 ZnO deposition Three different layers of ZnO were prepared: a compact layer deposited by spray pyrolysis (SP-ZnO) and two other layers where nanopillars of ZnO are electrodeposited, with and without chloride doping.

The compact SP-ZnO layer was deposited following the procedure described in detail elsewhere [21], either alone or between the glass and the nanopillars (to prevent pinholes). The spraying process included a total of 17 cycles. The solution was atomized using N$_2$ as a carrier gas in pulses: 2 seconds ON and 10 seconds OFF. The plate was heated at 425 ℃. After the last cycle was finished, the samples remained on the hot plate at 325℃ for 20 minutes.

The nanopillars were electrodeposited using a Voltalab PGP 201 potentiostat. A Zn foil served as counter electrode and a saturated calomel electrode (SCE) as reference electrode. All the potential values will be given against this reference. To prepare the nanopillars (NP-ZnO), aqueous solutions of 10 mmol L^{-1} Zn(NO$_3$)$_2$ at 70 °C and with constant stirring were used as electrolytic bath. The NP-ZnO layer was deposited by keeping the electrode at -1 V up to a total charge density of 1.33 Ccm^{-2}.

To dope with chlorides, 5 mmol L^{-1} NH$_4$Cl was incorporated to the electrolytic bath, so that the ratio between Cl$^-$ and Zn^{2+} in the precursor solutions, (Cl$^-$/Zn^{2+}) equals 0.5. These samples will be labelled as NP-Cl:ZnO.

2.3 In$_2$S$_3$ deposition The conditions for the sequential deposition of the buffer and absorbing layers were carefully chosen so that the previous one was preserved.

An ultrathin layer of In$_2$S$_3$ was deposited by spray pyrolysis in between the ZnO and the CuInS$_2$ layers. The deposition conditions followed those reported by other authors [24, 25].

The precursor solution contained 120mmol L^{-1} of thiourea and 18 mmol L^{-1} of InCl$_3$. The solution was atomized using N$_2$ as a carrier gas in pulses: 30 seconds ON and 60 seconds OFF. The plate was heated at 300 ℃. Six cycles were completed achieving a thickness of less than 100 nm. O'Hayre et al. have established an optimum thickness of 60 nm for this type of buffer layer [25]. After the last cycle, the samples remained on the hot plate at 300℃ for 30 minutes.

2.4 CuInS$_2$ (CIS) deposition CIS ink was prepared with slight variations from the methodology reported by Dehghani et al. [9]. Briefly, 0.105 mmol of CuCl, 0.1 mmol of InCl$_3$ and 0.4 mmol of thiourea were added to a mixture of acetic acid (0.046 mL) and *N*-propylamine (0.6 mL). The precursor solution was stirred using an ultrasonic bath for 30 minutes until it became light-brown.

The precursor ink was deposited onto FTO/ZnO/In$_2$S$_3$ by spin-coating at 2000 rpm for 20s. Two cycles were completed. After each cycle, the samples were kept on a hot plate at 150°C for 10 min to eliminate the solvent. Finally, the samples were kept on the hot plate at 250°C for 10 more minutes. During this last heat treatment, the color of the film changed from colorless to shiny black.

2.5 Characterization X-ray diffractograms were registered using a PANalytical X'Pert Pro diffractometer, with Cu-Kα radiation at 40 kV and 40 mA. The samples were scanned using the Brag Brentano configuration, between 20° and 80° at 0.02°/s. The crystallographic data were interpreted with X´Pert High Score software.

The morphology of each layer was recorded by scanning electron microscopy (SEM), using a JEOL JSM-5900LV microscope.

Localized Raman spectra were recorded with an Invia Reflex confocal Raman microprobe in backscattering configuration and using a 50x objective. Excitation was provided with a continuous-wave 785 nm laser.

The thickness of each layer and that of the cells was evaluated using a KLA TENCOR D-100 profilometer and compared with SEM cross-section and 45° images.

The optical properties of these cells were studied by transmittance spectroscopy using a double beam UV–VIS spectrophotometer Shimadzu UV-160.The transmittance was measured for all the samples using glass/FTO substrate as reference.

Current–voltage curves were recorded in the dark and under simulated solar irradiation using an IVIUM® compact potentiostat. Eight graphite dots of 0.003 cm^2 (effective area of the solar cell) were painted with conductive graphite ink (Alpha Aesar) using a mask on each sample and used as back contacts. The procedure was repeated for three samples of each specimen, giving a total of 24 spots per solar cell type. The light source was a 150 W Xe lamp coupled to an air-mass filter 1.5G (solar simulator, Oriel-Newport 96000). The light intensity was set at 100 mW cm^{-2} (1 Sun) with a calibrated Si photodiode.

The same graphite dots were used to measure the intensity modulated photovoltage and photocurrent spectroscopy (IMVS and IMPS respectively). These techniques, which have been mainly used earlier to characterize liquid/solid interfaces [26], are also being used to study cells in the solid state and require that the samples are excited with a modulated intensity optical signal. A red LED (639 nm, ~ 1 mW) was used as a source of optical excitation. The LED intensity and modulation was kept at the lowest possible values that give a measurable signal in order to diminish nonlinear effects. The frequency of the optical modulation was changed while the amplitude of the signal was kept constant, and with this configuration various frequency sweeps were performed from 1 Hz to 90 kHz. Repeatability was assured when the different sweeps overlapped on the same locus. The modulation was performed by a signal generator (Tecktronix AFG 3022B). Two lock-in amplifiers (Stanford Research Systems SRS-530) were used to detect the modulated signals (photocurrent or photovoltage), and the signal from a photodiode (UV Enhanced Silicon Detector) used to monitor the LED signal. This signal is used to avoid spurious intensity fluctuations and to normalize between the different measurements.

For the IPCE (Incident photon to current efficiency) characterization a 50 W halogen lamp (Newport 6337) was used as a source of white light excitation, which was monochromatized (ORIEL 77250) and chopped (SR 540) before reaching the sample. The electric contacts were the same graphite spots as previously described and the current signal (in short circuit condition) was detected by a Lock-in amplifier (SRS SR530). For the reference signal in this measurement, a calibrated Oriel 91150V reference cell was used.

3 Results and discussion This work describes a comparison between the performances of three different cells prepared in superstrate configuration by using various solution-based methodologies. In every case, the cells are supported on conductive glass (FTO, F:SnO$_2$), followed by the sequential deposition of a ZnO as window layer, a In$_2$S$_3$ as buffer layer and CIS as absorbing layer. The difference among the three cells relies on the morphology and composition of ZnO, since this layer can be sprayed as a dense layer (SP) or electrodeposited as nanopillars (NP). In turn, the nanopillars can be doped with chlorides (NP-Cl:ZnO). Cl incorporation was confirmed by Electron Dispersion Spectroscopy (EDS), X-rays Diffraction and UV-Vis Spectroscopy, as described elsewhere [21].

These diverse materials can be combined to prepare the three different cells summarized below:

Solar Cell 1 (SC1): FTO / SP-ZnO / In$_2$S$_3$ / CIS/ graphite
Solar Cell 2 (SC2): FTO / SP-ZnO / NP-ZnO / In$_2$S$_3$ / CIS/ graphite
Solar Cell 3 (SC3): FTO / SP-ZnO / NP-Cl:ZnO / In$_2$S$_3$ / CIS/ graphite

SEM images were recorded to follow the morphology of the layers as the deposition sequence progressed. Figures 1a to 1e display top-view images of (a) SP-ZnO, (b) SP-ZnO / In$_2$S$_3$/ CIS, (c) SP-ZnO / NP-ZnO, (d) SP-ZnO / NP-ZnO / In$_2$S$_3$ and (e) SP-ZnO / NP-ZnO / In$_2$S$_3$ / CIS. Figure 1f presents a cross-section image of SC2.

Images 1a and 1b correspond to the sequence of building SC1. The films are compact with spherical grains completely covering the substrate. Images 1c to 1e correspond to the sequence followed to build SC2. From Fig. 1c it can be seen that the nanopillars grown on SP-ZnO are densely packed and aligned, showing a well-defined hexagonal cross-section. Then, as can be observed in Fig. 1d, the hexagonal surface of the nanopillars fades away, which is a complementary evidence for the homogeneous deposition of the In$_2$S$_3$ ultra-thin layer that copies the morphology of the nanopillars. Finally, two cycles of spin coating with CIS are sufficient for the nanopillars to end up embedded in the absorbing layer. This can be seen in Fig. 1e, which corresponds to SC2. The film is homogeneous, shows no cracks and is relatively porous. The sequential

images corresponding to SC3 (not shown) are similar to those presented for SC2.

Figure 1f shows a cross-sectional view of SC2 cell. The global thickness resulting in values ranging from 1 to 1.5 μm. These values were confirmed by profilometry.
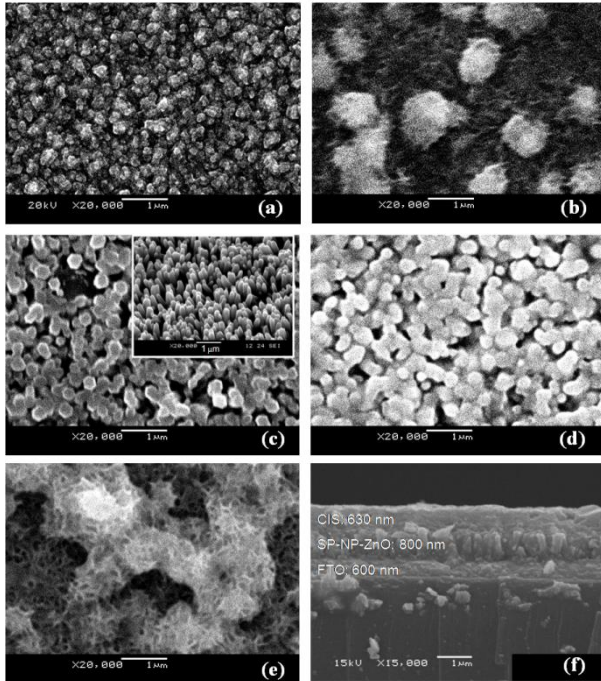
Figure 1: SEM micrographs showing the various layers involved in the solar cells: (a) SP-ZnO, (b) SP-ZnO / In$_2$S$_3$ / CIS (c) top and 45° inclined views of SP-ZnO / NP-ZnO (d) SP-ZnO / NP-ZnO / In$_2$S$_3$, (e) SP-ZnO / NP-ZnO / In$_2$S$_3$ / CIS and (f) cross sectional view of (e).

X-rays diffractograms (XRD) of the three cells were registered and two of them are presented in Figure 2. The diffraction patterns from each individual layer deposited on FTO substrate are shown as references to identify the corresponding peaks in SC1 and SC3. For SC1, the main peak of ZnO corresponds to the (101) plane at 36.2° indicating the presence of wurtzite (PDF 79-0207). There is also one broad weak peak at 27.9° that can be attributed to a chalcopyrite structure of CIS (PDF 27-0159). As this layer is very thin, the presence the absorber needs to be confirmed by Raman spectroscopy.

XRD of solar cells SC2 and SC3 are very similar, so only SC3 will be shown. In SC3, almost all the diffraction peaks corresponding to ZnO can be seen. There is a marked increment of the (002) peak which can be explained by the preferential orientation along the *c* axis, typical of the nanopillars. Again, one broad weak peak at 27.9° can be attributed to CIS. Unfortunately, the In$_2$S$_3$ buffer layer cannot be detected in the cell by XRD due to the ultrathin thickness.
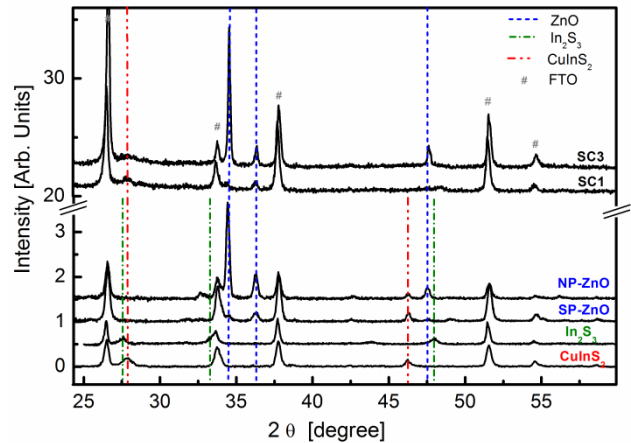
Figure 2: X-rays diffractograms corresponding to SC1, SC3, NP-ZnO, SP-ZnO, In$_2$S$_3$ and CuInS$_2$.

As a result of the different penetration of the incident radiation, Raman spectroscopy has been used to complement results from XRD. In the case of CIS, quasi-resonant Raman scattering measurements were performed, given that the excitation wavelength (785 nm) is close to the band gap of the compound under analysis [27]. Therefore, a strong increment in the intensity of the Raman modes can be achieved.

Figure 3 shows the spectra of cells SC1 (dotted curve) and SC3 (full line). The figure also shows the spectra recorded using a thick layer of CIS (dot-dashed curve) deposited directly on FTO using 5 instead of just 2 cycles, but in identical conditions. All of them are characterized by the presence of peaks in the 200–400 cm^{-1} spectral region. The peak centered at 270 cm^{-1} correspond to the B$_2$ mode of the chalcopyrite (CH) structure.The strong band at 307 cm^{-1} corresponds to the A$_1$ mode of the Cu–Au (CA) ordering polytype [27]. This is an indication that the film is a mixture of CH and CA orders.In resonant conditions, the band at 340 cm^{-1} corresponds to the presence of the B$_2^{(3)}$(L)/E$^{(6)}$(L) CuInS$_2$ mode. The presence of these signals in SC1 and SC3 confirms the presence of CIS, which was not clearly visible in the XRD patterns (Figure 2).
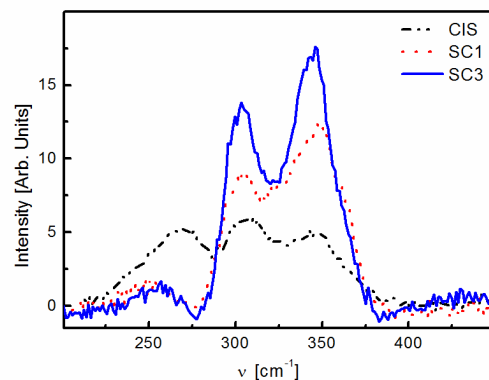
Figure 3: Typical Raman spectra taken from CIS, SC1 and SC3.

Figure 4 shows the optical transmittance of SC2 (full line) using as reference a bare FTO/glass substrate. In order to account for the influence of each individual layer on the overall transmittance of SC2, their transmittance spectra are also included in this figure. Each individual layer was deposited directly over a FTO/glass substrate. Interference oscillations present in both the FTO/glass substrate [28, 29] and the SP-ZnO layer could lead to an increase in the interference phenomena in the SP-ZnO transmittance spectra, explaining transmittance values above 100% [21]. These interference oscillations are expected due to the compact nature of the SP-ZnO layer, and its effect is reduced as the number of layers is increased [28].

The SP-ZnO transmittance spectra also shows the typical sharp direct-like absorption edge of ZnO thin films located at 380 nm [29]. The SP-ZnO/NP-ZnO spectrum (dot-dashed curve) also presents the ZnO absorption edge previously described and a smooth monotonous increment for longer wavelengths caused in the light scattering properties of the sample [30]. The transmittance of the buffer layer (dotted curve) shows an absorption edge located at 490 nm. The $CuInS_2$ layer shows the smallest transmittance (short dashed curve) of all, with a smooth increase for wavelengths higher than 700 nm corresponding to the absorption edge of $CuInS_2$. Finally, the optical transmittance of the whole SC2 cell (full line) clearly shows the absorption edges of both the ZnO and In_2S_3 layers. Less evident, but still present, is the $CuInS_2$ layer. The differences between the transmittance of the various layers and the transmittance corresponding to SC2 are caused by the different number of cycles used for the samples under study. In particular, In_2S_3 and $CuInS_2$ samples were prepared using more cycles than those used for the corresponding samples in SC2 cell. In order to get well-defined spectra, 18 and 5 cycles of deposition were used to grow these layers, respectively. Therefore, although with different relative weights, the spectrum of SC2 presents almost every absorption edge from the different materials.
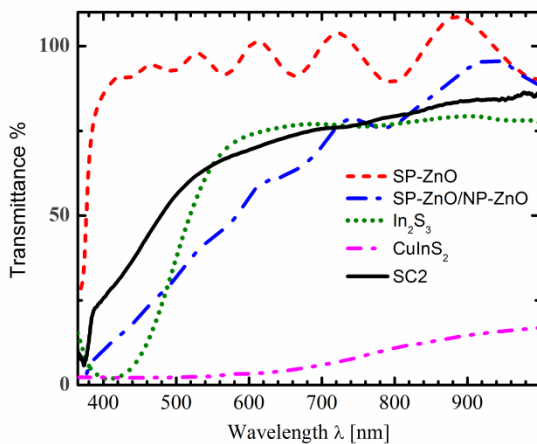

Figure 4: Transmittance spectra for samples: SP-ZnO (dashed line), SP-ZnO/NP-ZnO (long dash dot line), In_2S_3 (short dash dot line), CIS (dotted line) and SC2 (full line).

The bandgap energy (E_g) of each individual layer may be obtained from the absorption edge position and is presented in Table 1. As a direct bandgap is expected, the determination of the E_g values was made from the extrapolation to zero absorption of a linear fitting of $(\alpha h\nu)^2$ against photon energy ($h\nu$), where α is the experimental absorption coefficient [31-33]. First, an experimental absorptance was obtained, so that $\alpha_{exp} = -\ln T$. Then, a corrected absorptance (α_{corr}) was calculated as $\alpha_{corr} = \alpha_{exp} - \alpha_{back}$, where the background absorptance (α_{back}) adjusts for zero absorption. The dependence of α_{back} with $h\nu$ can be obtained from a linear fitting in the below gap region of the Tauc plot, where $(\alpha_{exp}h\nu)^{1/2}$ is plotted against $h\nu$. This is the same dependency used for amorphous and indirect semiconductors [33, 34]. The procedure of finding α_{back} was already used in similar nanostructured samples [28]. The correction is originated in the fact that scattering and spurious amorphous phases introduce uncertainty in the zero absorption line, which greatly influences the E_g values. In fact, this light scattering is responsible for the milky appearance of the NP-ZnO samples. Figures 5a and 5b show plots of $(\alpha_{corr}h\nu)^2$ against $h\nu$.

Table 1: Typical Eg values for each of the layers involved in the solar cells construction

Sample	E_g [eV]
SP-ZnO	3.26
SP-ZnO/ NP-ZnO	3.23
NP-ZnO Cl$^-$/ Zn^{2+} = 0	3.33
NP-Cl:ZnO Cl$^-$/ Zn^{2+} = 0.5	3.45
In$_2$S$_3$	2.65
CIS	1.65

The E_g values obtained for these samples were close to those expected for the bulk materials [1, 21, 24].In the particular case of SP-ZnO and SP-ZnO/NP-ZnO, both present similar values of E_g. This is because both layers consist of the same material, just with a different structure. For this reason, an optical characterization of NP-ZnO and NP-Cl:ZnO layers (without SP-ZnO) was carried out. Figure 5b shows a blue shift in the absorption edge of the NP-ZnO when doping with chloride. This behaviour is in accordance with previously reported shifts on the absorption edge with the Cl$^-$/Zn^{2+} ratio [21]. The shift is due to band filling effects (and eventual bandgap renormalization) originated in the excess of free electrons due to doping, i. e. Moss-Burstein effect [35].
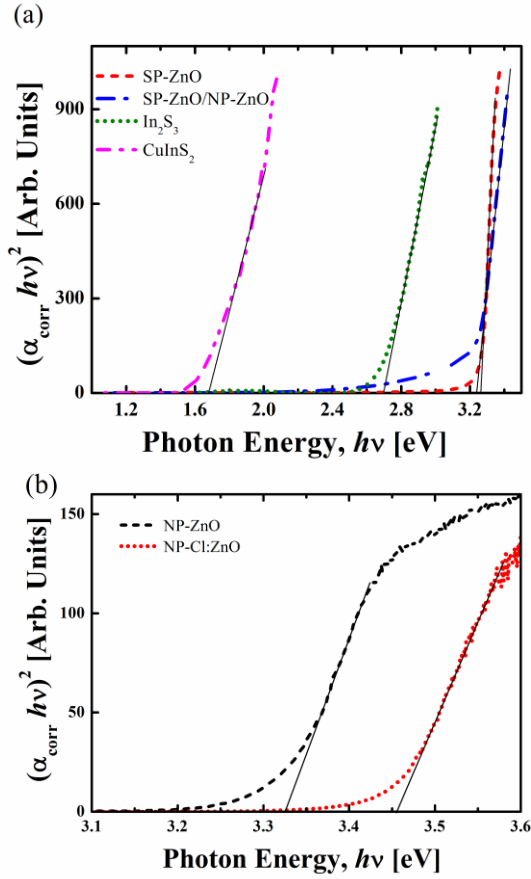
Figure 5: Plots for direct bandgap energy (Eg) determination for samples: (a) SP-ZnO (long dash line), SP-ZnO/NP-ZnO (dash dot line), In$_2$S$_3$ (dot line) and CuInS$_2$ (short dash line); (b) NP-ZnO (long dash line) and NP-Cl:ZnO (dot line)

Figure 6 presents the I-V curves registered for the best device of each cell in the dark and under illumination. No photoresponse could be detected in the absence of In$_2$S$_3$. The external cell parameters, namely the short-circuit current density (J_{SC}), open-circuit voltage (V_{OC}), fill factor (FF) and efficiency (η) can be calculated from those curves and are shown in Table 2. Other internal cell parameters, such as the series resistance (R_s) and shunt resistance (R_{sh}) were calculated from the J-V data recorded under illumination by linear fitting in different regions of the curves [36].

Even though the parameters and results of the best devices are shown to simplify the analysis, the mean values and standard deviation keep analogous trend. The standard deviation related with de mean values of the measured parameters (J_{sc}, V_{oc}, FF, η) are in all cases lower than 36%.

Table 2: Relevant electrical parameters for the best SC1, SC2, SC3 cells, derived from the results shown in Figures 6 and 7.

Sample	SC1	SC2	SC3
J_{SC} [mA cm^{-2}]	4.0	0.52	13.3
V_{OC} [V]	0.41	0.61	0.5
FF	0.27	0.2	0.43
η %	0.46	0.1	2.8
R_s [Ω cm^2]	3.3	77	0.9
R_{sh} [Ω cm^2]	111	860	79
τ_R [ms]	2.0	4.0	0.24
τ_D [ms]	0.82	0.84	0.02
η_{cc} %	59	79	92

The results show interesting differences among the various cells. The introduction of a nanostructured layer is not enough to produce a marked improvement in any of them and in fact the efficiency decreases when comparing SC1 to SC2. However, comparing SC2 to SC3 it is clear that when NP-ZnO is doped with chloride (NP-Cl:ZnO), the short-circuit current increases markedly. In turn, this translates into a much better energy conversion that increases from 0.1 to up to 2.8%.

Furthermore, it can be seen that the presence of a nanostructured layer tends to increase both resistances, R_s and R_{sh} (i. e. higher values for SC2 than SC1) but after Cl-doping (SC3) these values decrease again and end up being lower than for SC1.
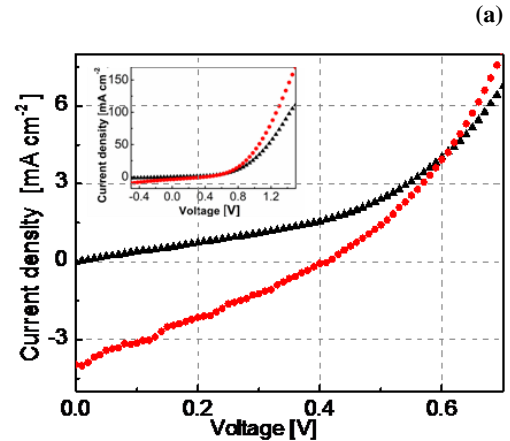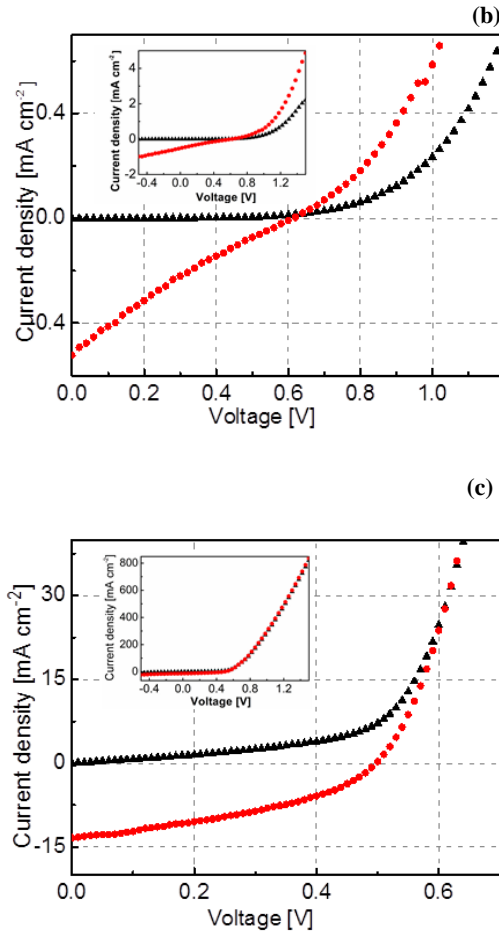
Figure 6: Current-voltage response of the three best cells in the dark (black triangle shape) and under simulated solar irradiation (red circle shape). (a) SC1; (b) SC2; (c) SC3. Relevant parameters are summarized in Table 2.

IMVS and IMPS frequency response measurements provide additional information on the internal dynamics of the cell. Both techniques require the excitation of electrons in the conduction band of the cell due to a small intensity optical modulated signal. Given that IMVS is performed at open-circuit conditions it is possible to explore the electron lifetime and electron-hole recombination dynamics [26], as in open-circuit conditions the excited electron-hole pair (inside the solid state cell in present case) can only return to the equilibrium condition by recombination. By means of IMPS measurements (at short circuit conditions), information about the combined effect of mass transport of the charge carriers and recombination could be obtained. If the charge collection process is faster than the recombination process, then the IMPS signal would lead to the characteristic time constant of the transport process (see below the time constant definitions)[26].

The characteristic electron recombination time (τ_R), electron transport time (τ_D), and charge collection efficiency

(η_{cc}) are important factors to estimate the overall performance of a solar cell. τ_R and τ_D can be obtained via Eq. (1) and Eq. (2), respectively [26, 37]:

$$\tau_R = \frac{1}{2\pi f_R} \qquad (1)$$

$$\tau_D = \frac{1}{2\pi f_D} \qquad (2)$$

where f_R and f_D are the frequency minima of the imaginary component in the IMVS and IMPS response, respectively. IMVS frequency response graphs for SC1, SC2 and SC3 are presented in Figure 7. These graphs are Nyquist plots of the response of the cell, i. e. imaginary part (quadrature component) against real part (in-phase component). The lines in Figure 7 are obtained by fitting the real and imaginary parts of IMVS response against frequency with the expression for a single time constant process [26]. The results for the time constant obtained from the fitting of the imaginary parts for each cell are summarized in Table 2.

The IMVS characteristic times obtained show that the lifetime or recombination time (τ_R) for SC1 and SC2 have the same order of magnitude. However, τ_R is much shorter for SC3. This can be expected due to the recombination rate increment originated by the defects states introduced by the doping. Also, the transport time (τ_D) calculated for SC3 cell is much shorter than those for cells SC1 and SC2, which are quite similar between them. This indicates a faster electron transport through SC3. This higher transport rate may be also originated in the Cl-doping, probably due to an increase of the band bending in the interface, ultimately acting as the driving force for charge separation. The reduced R_s [21] may also contribute to diminishing this transport time. Moreover, an increased overall mobility may contribute to a faster transport time of carriers through the device. For this reason the mobility of the nanopillars was calculated using previously measures of sheet resistivity and charge carrier densities [21]. The results give 9.7 cm^2 V^{-1} s^{-1} for NP-ZnO and 36 cm^2 V^{-1} s^{-1} for NP-Cl:ZnO. Therefore the mobility contribution on the whole transport across the device should be also considered.

Nevertheless, to weigh the electron transport and recombination processes combined, charge-collection efficiency, η_{cc} can be calculated according to the Eq. (3) [26]:

$$\eta_{cc} = 1 - \frac{\tau_D}{\tau_R} \qquad (3)$$

This is considered to be a more reliable parameter. The η_{cc} results are also displayed in Table 2. In general, a high η_{cc} value will result in high solar energy conversion, η; the cell SC3, which includes ZnO nanopillars doped with chloride exhibits the smallest τ_R and τ_D of all, and a higher charge collection efficiency (η_{cc}) than SC1 and SC2. All

of these results are in good agreement with the data derived from the previously studied current-voltage curves (Figure 6) and demonstrate the improvement introduced by the Cl-doping in the nanostructured layer.
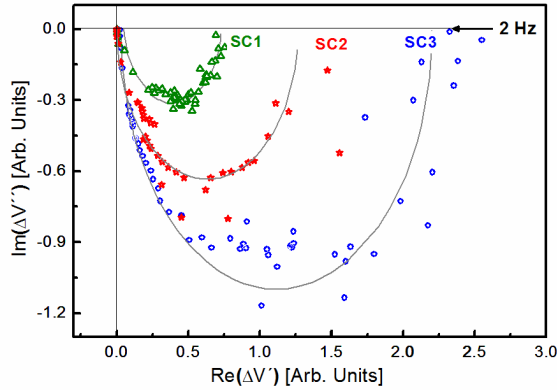
Figure 7: IMVS measurements of the three cells illuminated through the conducting substrate. Thin lines are fittings.

However, Table 2 shows a poor correspondence between the cell efficiency η and the charge collection efficiency η_{cc}. While SC2 has the smallest η, it has an intermediate value for η_{cc}. This may be related to the relative high series resistance R_s, and the departure of this cell from the single-diode model, which is not yet clearly understood.

Figure 8 shows the measured IPCE for samples SC1, SC2 and SC3.The current signal was chopped in order to be detected by the Lock-in amplifier. The chopping frequency used was smaller than the one obtained from the IMVS & IMPS characteristics frequencies of this sample. Towards the infrared region the signal is very small (almost zero). This indicates that there is almost no photoresponse originated in subbandgap (defect) states [38, 39]. As the photon energy is increased, the IPCE signal starts to grow smoothly. For higher energies the IPCE signal presents an abrupt decay. This decrease could be attributed to the absorption in the transparent conductor (ZnO). Once the absorption of ZnO becomes important, less photons are available for the charge carrier generation in the absorber, leading to a lower IPCE. The signal for the SC3 sample is the greatest of all, in accordance with its better performance (see Table 2). Moreover, both samples with NP (SC2 and SC3) have a greater IPCE in the visible region. This may be due to the light scattering capability of the NP [40]. The IPCE integrated short circuit current density was calculated. The values are 0.53, 0.72, and 2.0 mA cm^{-2} for samples SC1, SC2 and SC3 respectively. The discrepancy with the values on Table 2 may be due to uncertainty in the IPCE measurement caused by the degradation of the graphite contacts.
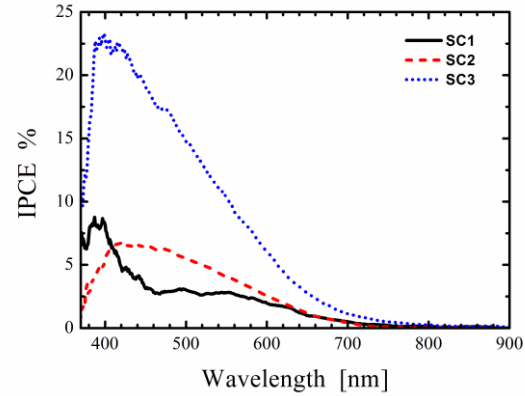
Figure 8: IPCE measurements for solar cells SC1, SC2 and SC3

4 Conclusions This work reports results from a novel nanostructured CIS solar cell in superstrate configuration, totally obtained from solution-processed deposition methods. The In$_2$S$_3$/CIS junction was impregnated into electrodeposited ZnO nanopillars by spray pyrolysis and spin coating from a precursor ink (CIS). The stacked layers were then annealed at low temperature to preserve the nanostructure.

Our best cell (SC3) is competitive with other superstrate cells produced by solution-based methodologies or nanostructuring strategies. It is worthwhile noting that this cell was prepared using simple, cost-effective and benign processes, avoiding vacuum, toxic materials, high temperature heat treatments, Cd-containing layers and KCN purification stages.

The mere introduction of a nanostructured layer was not enough to improve the photoresponse of the solar cell. The conversion efficiency of the solar cell increased considerably only when using Cl-doped nanopillars, attaining a maximum efficiency of 2.8%.

A better series resistance together with a higher value for the charge collection efficiency, contribute to explain the corresponding improvement in cell efficiency. This can also be verified from the IPCE measurement.

References

[1] J. Kaneshiro, N. Gaillard, R. Rocheleau, E. Miller, Sol. Energy Mater. Sol. Cells, **94**, 12-16 (2010).

[2] H. Azimi, Y. Hou, C.J. Brabec, Energy and Environ. Sci., **7**, 1829-1849 (2014).

[3] L. Li, T. Zhai, Y. Bando, D. Golberg, Nano Energy, **1**, 91-106 (2012).

[4] J. Huang, Z. Yin, Q. Zheng, Energy and Environ. Sci., **4**, 3861-3877 (2011).

[5] C. Broussillou, M. Andrieux, M. Herbst-Ghysel, M. Jeandin, J.S. Jaime-Ferrer, S. Bodnar, E. Morin, Sol. Energy Mater. Sol. Cells, **95**, S13-S17(2011).

[6] A.H. Cheshme Khavar, A. Mahjoub, F.S. Samghabadi, N. Taghavinia, Mater. Chem. Phys., **186**, 446-455(2017).

[7] A.H. Cheshme Khavar, A.R. Mahjoub, F. Tajabadi, M. Dehghani, N. Taghavinia, Eur. J. Inorg. Chem.,**2015**, 5793-5800(2015).

[8] A.H. Cheshme Khavar, A.R. Mahjoub, H. Fakhri, M. Dehghani, RSC Adv., **5**, 97381-97390(2015).

[9] M. Dehghani, A. Behjat, F. Tajabadi, N. Taghavinia, J. Phys. D: Appl. Phys., **48**, 115304(2015).

[10] D. Lee, K. Yong, J. Phys. Chem. C, **118**, 7788-7800 (2014).

[11] S.M. Lee, S. Ikeda, T. Yagi, T. Harada, A. Ennaoui, M. Matsumura, Phys. Chem. Chem. Phys., **13**, 6662-6669 (2011).

[12] T. Ryo, D.-C. Nguyen, M. Nakagiri, N. Toyoda, H. Matsuyoshi, S. Ito, Thin Solid Films, **519**, 7184-7188 (2011).

[13] N.D. Sankir, E. Aydin, E. Ugur, M. Sankir, J. Alloys and Compd., **640**, 468-474 (2015).

[14] M.H. Valdés, M. Berruet, A. Goossens, M. Vázquez, Surf. Coat. Technol., **204**, 3995-4000(2010).

[15] T. Zhang, Y. Yang, D. Liu, S.C. Tse, W. Cao, Z. Feng, S. Chen, L. Qian, Energ. Environ. Sci., **9**, 3674-3681(2016).

[16]E. Kärber, A. Abass, S. Khelifi, M. Burgelman, A. Katerski, M. Krunks, Sol. Energy, **91**, 48-58(2013).

[17] L. Tsakalakos, Mater. Sci. Eng. R., **62**, 175-189(2008).

[18] J.M. Spurgeon, H.A. Atwater, N.S. Lewis, J. Phys. Chem. C, **112**, 6186-6193(2008).

[19] R. Tena-Zaera, M.A. Ryan, A. Katty, G. Hodes, S. Bastide, C. Lévy-Clément, C. R. Chim., **9**, 717-729 (2006).

[20] J.B. Baxter, E.S. Aydil, App. Phys. Lett., **86**, 1-3 (2005).

[21] M. Berruet, D.L. Gau, E.A. Dalchiele, M. Vázquez, R.E. Marotti, J. Phys. D: Appl. Phys., **49**, 215103 (2016).

[22] H. Mönig, C.H. Fischer, R. Caballero, C.A. Kaufmann, N. Allsop, M. Gorgoi, R. Klenk, H.W. Schock, S. Lehmann, M.C. Lux-Steiner, I. Lauermann, Acta Mater., **57**, 3645-3651 (2009).

[23] C.J. Hibberd, E. Chassaing, W. Liu, D.B. Mitzi, D. Lincot, A.N. Tiwari, Prog. Photovoltaics: Res. Appl., **18**, 434-452 (2010).

[24] T. Sall, B. Marí Soucase, M. Mollar, B. Hartitti, M. Fahoume, J. Phys. Chem.Solids, **76**, 100-104(2015).

[25] R. O'Hayre, M. Nanu, J. Schoonman, A. Goossens, Nanotechnology, **18**, 055702(2007).

[26] G. Schlichthörl, N.G. Park, A.J. Frank, J. Phys Chem. B, **103**, 782-791 (1999).

[27] J. Álvarez-García, J. Marcos-Ruzafa, A. Pérez-Rodríguez, A. Romano-Rodríguez, J.R. Morante, R. Scheer, Thin Solid Films, **361**, 208-212(2000).

[28] C.D. Bojorge, V.R. Kent, E. Teliz, H.R. Cánepa, R. Henríquez, H. Gõmez, R.E. Marotti, E.A. Dalchiele, Phys. Status Solidi (A) Appl. Mater. Sci., **208,** 1662-1669 (2011).

[29] A. Tello, H. Gómez, E. Muñoz, G. Riveros, C.J. Pereyra, E.A. Dalchiele, R.E. Marotti, J. Electrochem. Soc., **159** (2012).

[30] L. Campo, E. Navarrete-Astorga, C.J. Pereyra, A. Cuevas, R. Romero, D. Ariosa, R. Henríquez, E. Muñoz, R.E. Marotti, F. Martín, J.R. Ramos-Barrado, E.A. Dalchiele, J. Electrochem. Soc., **163,** D392-D400(2016).

[31] J. Pankove, Optical Processes in Semiconductors, Dover Publications, 1971.

[32] B. Sapoval, C. Hermann, Physics of Semiconductors, Springer, 1995.

[33] O. Stenzel, The Physics of Thin Film Optical Spectra, Springer, 2005

[34] J. Tauc, Mater. Res. Bull., **5**, 721-729(1970).

[35] E. Burstein, Phys. Rev., **93**, 632-633(1954).

[36] C. Zhang, J. Zhang, Y. Hao, Z. Lin, C. Zhu, J. Appl. Phys., **110,**064504(2011).

[37]] X. Miao, K. Pan, Y. Liao, W. Zhou, Q. Pan, G. Tian, G. Wang, J. Mater. Chem. A, **1**, 9853 (2013).

[38] P. Guha, D. Das, A.B. Maity, D. Ganguli, S. Chaudhuri, Sol. Energy Mater. Sol.Cells, **80**, 115-130 (2003).

[39] A. Amara, W. Rezaiki, A. Ferdi, A. Hendaoui, A. Drici, M. Guerioune, J.C. Bernède, M. Morsli, Sol. Energy Mater. Sol. Cells, **91**, 1916-1921(2007).

[40] L. Campo, E. Navarrete-Astorga, C. J. Pereyra, A. Cuevas, R. Romero, D. Ariosa, R. Henríquez, E. Muñoz, R. E. Marotti, F. Martín, J. R. Ramos-Barrado, E. A. Dalchiele, J. Electrochem. Soc., **163** (8) D392-D400 (2016).